

## Article

# Evaluation of Electromagnetic Fields of Extremely Low-Frequency Horizontal Electric Dipoles at Sea–Air Boundaries

Sumou Hu , Hui Xie \* and Zhangming Li

College of Electronic Engineering, Naval University of Engineering, Wuhan 430033, China; m22181002@nue.edu.cn (S.H.); lizhangming\_007@163.com (Z.L.)

\* Correspondence: 0909031059@nue.edu.cn

**Abstract:** The technologies of undersea detection and communication, seabed sensor networks, and geophysical detection using electromagnetic waves have emerged as research focal points within the field of marine science and engineering. However, most studies have focused on the propagation of electromagnetic fields over long distances within the shallow “sea-seabed” environment. This paper introduces a quasi-static approximation method to address the Sommerfeld numerical integration challenge within the near-field region, employing the horizontal electric dipole (HED) as a model. It derives the Sommerfeld numerical integral expressions under conditions where the wave-number ratio at the “seawater-air” boundary does not adhere to the requirement of  $|k_0/k_1| \ll 1$  (where subscripts 0 and 1 denote seawater and air media, respectively). Building upon this, the paper simplifies the Bessel-Fourier infinite integral term within the integral expression to obtain Sommerfeld numerical integral approximations for the propagation of electromagnetic fields in the near region of extremely low frequency (ELF) within seawater. The study further conducts simulations and calculations to determine amplitude variations in electromagnetic field intensity generated by an ELF HED at different frequencies, dipole heights, and observation point depths. It concludes with an analysis of electromagnetic field propagation characteristics at the seawater-air boundary. Experimental findings highlight the lateral wave as the primary mode of electromagnetic wave propagation at this interface.

**Keywords:** extremely low frequency (ELF); horizontal electric dipole (HED); quasi-static approximation; Sommerfeld numerical integration



**Citation:** Hu, S.; Xie, H.; Li, Z. Evaluation of Electromagnetic Fields of Extremely Low-Frequency Horizontal Electric Dipoles at Sea–Air Boundaries. *Electronics* **2023**, *12*, 4165. <https://doi.org/10.3390/electronics12194165>

Academic Editor: Anna Richelli

Received: 3 September 2023

Revised: 6 October 2023

Accepted: 6 October 2023

Published: 7 October 2023



**Copyright:** © 2023 by the authors. Licensee MDPI, Basel, Switzerland. This article is an open access article distributed under the terms and conditions of the Creative Commons Attribution (CC BY) license (<https://creativecommons.org/licenses/by/4.0/>).

## 1. Introduction

Over the past few decades, the study of electromagnetic wave (EMW) propagation in layered media has attracted considerable attention [1–3], particularly in the context of EMW propagation across the sea-air interface. In comparison to techniques employed in acoustics [4,5] and optics [6,7], as well as other fields of ocean engineering, EMWs exhibit unique and valuable properties that render them a prime choice for applications in ocean communication engineering. Despite their limited transmission range owing to high attenuation, EMWs possess several advantageous features. Firstly, they can seamlessly traverse the “sea-air” interface, thereby extending the transmission range for both aerial and seabed paths. Secondly, electromagnetic transmission is resilient in the face of tidal waves and turbulence resulting from human activities. Thirdly, EMWs can operate effectively in turbid water conditions, among other advantages. Therefore, the utilization of EMWs in seawater environments has garnered significant interest in recent years [8–10].

The problem of dipole radiation in multilayered media was first introduced by Sommerfeld in 1909 [11]. Since then, this research area has witnessed substantial interest and notable achievements, finding applications in various engineering domains, including geophysical exploration [12], submarine communication [13], underwater navigation [14], and submarine detection and communication [15,16]. Much of the subsequent work builds

upon Sommerfeld's integral [11], which serves as the theoretical foundation for the propagation and scattering of EMW. However, in this context, calculating the electromagnetic field (EMF) necessitates solving the challenging Sommerfeld integral due to its singularity and high oscillation near the integration path. Margetis [17] and Banos [18] significantly advanced the theory of dipole sources embedded in conductive half-spaces, obtaining approximate solutions for different distances from the source. Numerous other scholars have also made substantial contributions to the analysis of EMF in layered conductive media [19–22]. Among them, the description and explanation of the physical process of EMW propagation across the sea–air interface is a topic of interest. In a study by Bush et al. (2012) [23], the propagation path of EMWs between transmitting and receiving antennas located in seawater was investigated. The study proposed that the propagation path consists of direct wave, reflected wave, and lateral wave propagation, as shown in Figure 1, and provided the analytical expression for the related components.

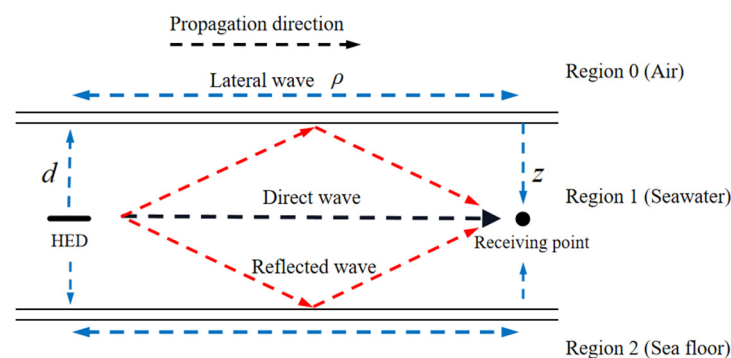


**Figure 1.** Schematic diagram of low-frequency field propagation from source to receiving point in seawater.

Bishay (2013) [24] utilized complex image theory [25] and the Hankel transform (integral over the radial distance  $r$ ) [26] to calculate the far field of the electric field disturbance caused by a vertical electric dipole (VMD) in seawater. A good approximate solution for the far field was obtained. Wang (2015) [27] derived the analytical expression of the EMF generated by a dipole antenna in the three-layer medium consisting of air, seawater, and seabed. Numerical calculations were performed using the fast Fourier transform (FFT) method to obtain the variation and spatial distribution of the EMF in the air with distance. The study confirmed that underwater EMWs primarily rely on air distance for long-distance transmission. Wang and Li (2017) [28] comprehensively analyzed the airborne EMF generated by a horizontal electric dipole (HED) in shallow seawater through theoretical analysis and experimental verification. The study proved that low frequency and interface effects are crucial for achieving long-distance transmission. In the extremely low frequency (ELF) band, EMWs can travel over 3 km on the sea surface with reasonable transmission power. Subsequently, Xu (2018) [29] investigated the near-field propagation of ELF waves excited by HED near the boundary between seawater and seafloor. The study proposed the use of the MacLaurin expansion method to derive an analytical solution for the near-field of the seafloor under quasi-static approximation conditions. Peng (2018) [30] discussed the calculation of the electric field radiated by a horizontal magnetic dipole (HMD) antenna into a lossy half-space, simulating it as a two-layer medium. The study derived a set of EMF expressions composed of Sommerfeld-type integrals under quasi-static magnetic field conditions. Shoeiba (2020) [31] considered the EMF generated by VMD under seawater in a planar three-layer conductive media (air, seawater, and seabed) and theoretically demonstrated that underwater VMD performs better when EMWs propagates through the boundary. The experiment verified that the depth and frequency of the transmitter significantly affect wave propagation in each region, with increased transmitter depth leading to a rapid reduction in the radiation field in the air. In the range of 50 m, changes in receiver height have a negligible influence on-field intensity, particularly in the far field.

Zeng (2021) [32] studied the modal theory of ELF wave propagation in layered marine lithospheric waveguides using surface impedance boundary conditions. The study derived the modal equations for transverse magnetic polarization guiding modes and transverse electric polarization guiding modes and obtained analytical expressions for propagatable modal parameters such as phase velocity, decay rate, excitation factor, and field strength under different components. Based on the conditional assumption of  $\gamma_1 \gamma_0 \gg k_1^2$  (where  $\gamma$  is the propagation constant and  $k$  is the wave number, subscripts 0 and 1 represent seawater and air, respectively), Xu (2021) [33] mainly derived the complete and effective solution for the electromagnetic near field generated by VMD on the sea surface in the air and seawater region under cylindrical coordinates. Hu (2023) [34] also utilized the McLaughlin expansion method to solve the near-field analytical solution under the quasi-static approximation condition at the uniformly infinite sea-air boundary. The study provided the spatial radiation distribution changes of the EMF but did not analyze the EMF propagation characteristics in different environments at the sea-air boundary.

In general, these limited studies underscore the analytical challenges posed by the Sommerfeld integral in the context of near-field wave propagation, particularly due to the presence of interfaces. In situations where an ELF wave propagates along the boundary of two media with a propagation distance of  $k\rho \ll 1$ , the Fourier–Bessel integral term in the Sommerfeld integral expression exhibits a divergence near the pole of  $k\rho \rightarrow 0$  at the seawater–air interface. For example, when EMWs propagate at the “sea-air” field interface, the ratio of ELF electromagnetic wave numbers denoted as  $k_1/k_0$  tends toward infinitesimal values. Margetis’s integral expression [17] can calculate the near-region EMF when  $k_1\rho \ll 1$ . However, when an ELF wave propagates along the sea-air interface, the dielectric constant of seawater can be approximated as purely imaginary ( $\epsilon_{sea} \approx j\sigma\omega$ ), and  $|k_1/k_0| \ll 1$  is not met. Consequently, Margetis’s method is unsuitable for near-region propagation issues. Conversely, numerical calculation methods [35,36] offer limited resolution, unable to provide a practical means of evaluating radiation intensity near the source and presenting difficulties or impossibilities in addressing near-field regions.

ELF, with an operating frequency range of 3–30 Hz, boasts an exceptionally long wavelength, approaching the circumference of the Earth—approximately three-quarters of it. When the field point and the source point are not significantly distant, the EMF propagation problem in the near-field of the HED becomes a pertinent subject of study. This paper delves into the EMF propagation in the near-field excited by an ELF HED at the sea-air interface, utilizing the HED model. To address this issue, we propose the use of the Sommerfeld numerical integral calculation method under quasi-static approximation conditions, specifically  $\omega \rightarrow 0$ ,  $k_1\rho \ll 1$ ,  $k_1 \ll k_0$ . Building upon this, we simplify the approximate numerical results of the Bessel-Fourier infinite integral term in the Sommerfeld integral expressions, leading to derived approximate integral expressions for EMF propagation in the near-region of seawater. To ascertain the validity of our proposed method, we compare its calculation results with those of Margetis [17] and Pan [22]. Furthermore, through simulation, we calculate and analyze the EMF propagation characteristics at the sea-air interface across different frequencies, dipole source heights, and observation point heights. These findings hold practical value in the realms of underwater target detection, underwater communication, and underwater navigation.

## 2. EMF Propagation Model in ELF at the Sea-Air Boundary

The model for the propagation of ELF EMF in the sea-air boundary, excited by a HED, is illustrated in Figure 2. We employ cylindrical coordinates as the reference system. Let us consider the HED positioned at the air-sea interface ( $z = 0$ ), with the dipole directed downward along the positive  $z$ -axis and parallel to the  $x$ -axis ( $\varphi = 0^\circ$ ). The distance from the  $xoy$  plane, representing the sea surface, is denoted as “ $d$ ” meters, and the electric moment is represented by “ $Idl$ ”. The observation point, labeled as  $P(\rho, \varphi, z)$ , is situated at a height “ $z$ ” meters above the sea surface.

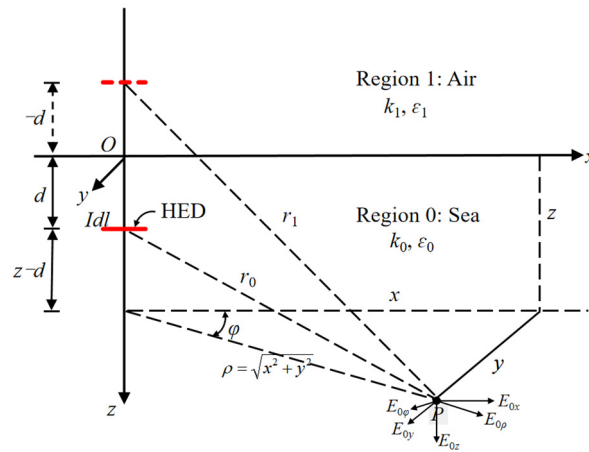


**Figure 2.** EMF propagation model of HED source excitation in seawater in a cylindrical coordinate system.

As depicted in Figure 2, the upper half-space is filled with air, referred to as region 1 ( $z < 0$ ), with respective electrical parameters denoted as  $k_1, \mu_1, \sigma_1$ , and  $\epsilon_1$ . The lower half-space is occupied by seawater, termed region 0 ( $z \geq 0$ ), with electrical parameters labeled as  $k_0, \mu_0, \sigma_0$ , and  $\epsilon_0$ . We define “ $\rho$ ” as the propagation distance between the projection point of the electric dipole source and the observation point, “ $r_0$ ” as the geometric distance from the electric dipole source point to the observation point in seawater, and “ $r_1$ ” as the geometric distance from the mirrored electric dipole source point to the observation point in air. For ELF electric dipole excitation varying with the time-harmonic factor  $e^{-j\omega t}$ , the EMF it generates in seawater region 0 ( $z \geq 0$ ) can be expressed as an integral [11], as comprehensively demonstrated in Appendix A. In this paper, we use the electric field component  $E_{0\rho}$  and the magnetic field component  $B_{0\rho}$  from [11] for illustrative purposes.

$$E_{0\rho} = -\frac{\omega\mu_0 Idl}{4\pi k_0^2} \cos \varphi \int_0^\infty \left\{ k_0^2 J_0(\lambda\rho) - \frac{\lambda^2}{2} [J_0(\lambda\rho) - J_2(\lambda\rho)] \right\} \gamma_0^{-1} e^{j\gamma_0|z-d|} \lambda d\lambda + \int_0^\infty \left\{ \frac{\gamma_0 M}{2} [J_0(\lambda\rho) - J_2(\lambda\rho)] - \frac{k_0^2 N}{2\gamma_0} [J_0(\lambda\rho) + J_2(\lambda\rho)] \right\} e^{j\gamma_0(z+d)} \lambda d\lambda \quad (1)$$

$$B_{0\rho} = -\frac{\mu_0 Idl}{4\pi} \sin \varphi \left\{ \pm \int_0^\infty J_0(\lambda\rho) e^{j\gamma_0|z-d|} \lambda d\lambda + \int_0^\infty \left\{ \frac{M}{2} [J_0(\lambda\rho) + J_2(\lambda\rho)] - \frac{N}{2} [J_0(\lambda\rho) - J_2(\lambda\rho)] \right\} e^{j\gamma_0|z+d|} \lambda d\lambda \right\} \quad (2)$$

where

$$k_0^2 = \left( \epsilon_0^{1/2} \frac{\omega}{c} \right)^2 \quad (3)$$

$$\gamma_n^2 = k_n^2 - \lambda^2 \quad n = 0, 1, \dots \quad (4)$$

$$M = \frac{k_0^2 \gamma_1 - k_1^2 \gamma_0}{k_0^2 \gamma_1 + k_1^2 \gamma_0} \quad (5)$$

$$N = \frac{\gamma_1 - \gamma_0}{\gamma_1 + \gamma_0} \quad (6)$$

Here,  $\gamma_0$  represents the propagation parameter in region 0,  $\gamma_1$  represents the propagation parameter in region 1,  $\omega$  is the angular frequency,  $\lambda$  is the wavelength,  $c$  is the speed of light in free space, and  $j$  is the imaginary unit.  $J_n(\lambda\rho)$  is a Bessel function of order  $n$ , with  $n = 0, 1, 2$ .

### 3. Quasi-Static Approximation

#### 3.1. Assumptions

In our “sea-air” half-space model, the electrical parameters of seawater and air exhibit significant disparities ( $k_1 \ll k_0$ ). Under the condition that the propagation distance satisfies  $k_1\rho \ll 1$ , particularly near the boundary of the two media layers (i.e.,  $d \ll \rho$  and  $z \ll \rho$ ), we encounter discrete terms in the Sommerfeld integral expression of the Bessel–Fourier function near the pole at  $k_1\rho \rightarrow 0$ . This makes it challenging to accurately calculate the variation in EMF intensity. However, within the infinite homogeneous medium of seawater, the near-field ELF EMF adheres to the “quasi-static” hypothesis, allowing us to simplify the following relationship:

$$\begin{cases} \gamma_0 = \sqrt{k_0^2 - \lambda^2} = \lim_{\omega \rightarrow 0} \sqrt{\left(\frac{\epsilon_0^{1/2}}{c}\omega\right)^2 - \lambda^2} \approx j\lambda \\ \gamma_1 = \sqrt{k_1^2 - \lambda^2} = \lim_{\omega \rightarrow 0} \sqrt{\left(\frac{\epsilon_1^{1/2}}{c}\omega\right)^2 - \lambda^2} \approx j\lambda \end{cases} \quad (7)$$

$$M = \frac{k_0^2\gamma_1 - k_1^2\gamma_0}{k_0^2\gamma_1 + k_1^2\gamma_0} \approx 1 \quad (8)$$

$$N = \frac{\gamma_1 - \gamma_0}{\gamma_1 + \gamma_0} \approx 0 \quad (9)$$

By substituting Equations (7)–(9) into Equations (1) and (2), we can simplify the electric field component  $E_{0\rho}$  and magnetic field component  $B_{0\rho}$  as follows:

$$E_{0\rho} = -\frac{Idl}{4\pi\sigma_0} \cos \varphi \int_0^\infty \left\{ \frac{1}{2} [J_0(\lambda\rho) - J_2(\lambda\rho)] \right\} \cdot [e^{-\lambda|z-d|} + e^{-\lambda|z+d|}] \lambda^2 d\lambda \quad (10)$$

$$B_{0\rho} = -\frac{\mu_0 Idl}{4\pi} \sin \varphi \left\{ \pm \int_0^\infty J_0(\lambda\rho) e^{-\lambda|z-d|} \lambda d\lambda + \int_0^\infty \left\{ \frac{1}{2} [J_0(\lambda\rho) + J_2(\lambda\rho)] \right\} e^{-\lambda(z+d)} \lambda d\lambda \right\} \quad (11)$$

The plus and minus signs in Equation (11) correspond to  $z > d$  and  $0 < z \leq d$ , respectively.

#### 3.2. Bessel-Fourier Integral Solution

Given that each component of the EMF’s simplified expression involves an infinite integral term of the Bessel function, direct calculation of changes in EMF intensity distribution in seawater becomes impractical. Therefore, we need to further simplify the integral expression for each field component, which can be achieved by consulting the integral table [37]. The Bessel-Fourier integral terms for other EMF component integral expressions are provided in Appendix B.

$$A_1(z, \rho) = \int_0^\infty J_0(\lambda\rho) e^{-\lambda z} \lambda d\lambda = \frac{z}{R^3} \quad (12)$$

$$A_2(z, \rho) = \int_0^\infty J_1(\lambda\rho) e^{-\lambda z} \lambda d\lambda = \frac{\rho}{R^3} \quad (13)$$

where  $R = \sqrt{\rho^2 + z^2}$ . Meanwhile, we derived the following integral:

$$A_3(z, \rho) = \int_0^\infty \frac{1}{2} [J_0(\lambda\rho) + J_2(\lambda\rho)] e^{-\lambda z} \lambda^2 d\lambda \quad (14)$$

where

$$\begin{aligned} f(z, \rho) &= \frac{1}{\rho} \int_0^\infty J_1(\lambda\rho) e^{-\lambda z} d\lambda \\ \frac{df(z, \rho)}{dz} &= -\int_0^\infty J_1(\lambda\rho) e^{-\lambda z} d\lambda = -A_2(z, \rho) = -\frac{\rho}{R^3} \end{aligned} \quad (15)$$

Therefore,

$$f(z, \rho) = \int_{-\infty}^z A(t, \rho) dt = -\rho \int_{-\infty}^z \frac{1}{(t^2 + \rho^2)^3} dt = \frac{1}{\rho} \left(1 - \frac{z}{R}\right) \tag{16}$$

Then,

$$A_3(z, \rho) = \frac{1}{\rho^2} \left(1 - \frac{z}{R}\right) \tag{17}$$

For Equations (15)–(17),  $\rho = 0$  is not a singularity because as  $\rho$  tends to 0,

$$\left(1 - \frac{z}{R}\right) = \left(1 + \frac{\rho^2}{z^2}\right)^{-\frac{1}{2}} = -\frac{\rho^2}{2z^2} + \frac{3\rho^4}{8z^4} \dots \tag{18}$$

Therefore,

$$A_3(z, \rho) \approx \frac{1}{2z^2} - \frac{3\rho^2}{8z^4} \dots \tag{19}$$

Through actual calculation, we can obtain

$$A_3(z, \rho) = \begin{cases} \frac{1}{\rho^2} \left(1 - \frac{z}{R}\right) & \rho/z > 0.1 \\ \frac{1}{2z^2} - \frac{3\rho^2}{8z^4} & \rho/z \leq 0.1 \end{cases} \tag{20}$$

$$\begin{aligned} A_4(z, \rho) &= \int_0^\infty \frac{1}{2} [J_0(\lambda\rho) - J_2(\lambda\rho)] e^{-\lambda z} \lambda^2 d\lambda = \frac{d}{d\rho} \int_0^\infty J_1(\lambda\rho) e^{-\lambda z} \lambda d\lambda \\ &= \frac{d}{d\rho} \frac{\rho}{R^3} = \frac{1}{R^3} \left(1 - \frac{3\rho^2}{R^2}\right) \end{aligned} \tag{21}$$

By incorporating Equations (12), (20), and (21) into Equations (10) and (11), we can further simplify the integral expressions for the electric field component  $E_{0\rho}$  and magnetic field component  $B_{0\rho}$  in seawater:

$$\begin{aligned} E_{0\rho} &= -\frac{Idl}{4\pi\sigma_0} \cos \varphi \int_0^\infty \left\{ \frac{1}{2} [J_0(\lambda\rho) - J_2(\lambda\rho)] \right\} \cdot [e^{-\lambda|z-d|} + e^{-\lambda|z+d|}] \lambda^2 d\lambda \\ &= -\frac{Idl}{4\pi\sigma_0} \cos \varphi \left[ \frac{1}{r_1^3} \left(1 - \frac{3\rho^2}{r_1^2}\right) + \frac{1}{r_0^3} \left(1 - \frac{3\rho^2}{r_0^2}\right) \right] \end{aligned} \tag{22}$$

$$\begin{aligned} B_{0\rho} &= -\frac{\mu_0 Idl}{4\pi} \sin \varphi \left\{ \pm \int_0^\infty J_0(\lambda\rho) e^{-\lambda|z-d|} \lambda d\lambda + \int_0^\infty \left\{ \frac{1}{2} [J_0(\lambda\rho) + J_2(\lambda\rho)] \right\} e^{-\lambda(z+d)} \lambda d\lambda \right\} \\ &= \begin{cases} -\frac{\mu_0 Idl}{4\pi} \sin \varphi \left[ \frac{z-d}{r_1^3} + \frac{1}{\rho^2} \left(1 - \frac{z+d}{r_0}\right) \right] & \frac{\rho}{z+d} > 0.1 \\ -\frac{\mu_0 Idl}{4\pi} \sin \varphi \left[ \frac{z-d}{r_1^3} + \frac{1}{2(z+d)^2} - \frac{3\rho^2}{8(z+d)^4} \right] & \frac{\rho}{z+d} \leq 0.1 \end{cases} \end{aligned} \tag{23}$$

Similarly, we can simplify the solution to determine components of the EMF at other points, as detailed in Appendix C.

### 3.3. Verification and Analysis

To ascertain the validity of the method presented in this paper, we simplified the approximate expression provided by Pan [22] and the exact expression from Margetis [17] using MacClaurin’s progressive formula. Subsequently, we compared the calculated results of these simplified expressions with those derived from the method proposed in this

paper. We selected scenarios where both the observation point and the emission dipole source were situated on the sea surface ( $\varphi = 0^\circ$ ). The conductivity of seawater was set at  $\sigma_0 = 4 \text{ S/m}$ , the relative dielectric constant at  $\epsilon_0 = 80$ , and the relative dielectric constant of the air layer at  $\epsilon_1 = 1$ . To rigorously test the accuracy of our proposed method, we focused on representative electric field intensities at the lowest frequency of 3 Hz and the highest frequency of 30 Hz within the ELF band. Figure 3a,b depict the comparisons between the calculated results obtained through our proposed method and existing results for the electric field component  $E_{0\rho}$  at the operating frequencies of  $f = 3 \text{ Hz}$  and  $f = 30 \text{ Hz}$ , respectively.

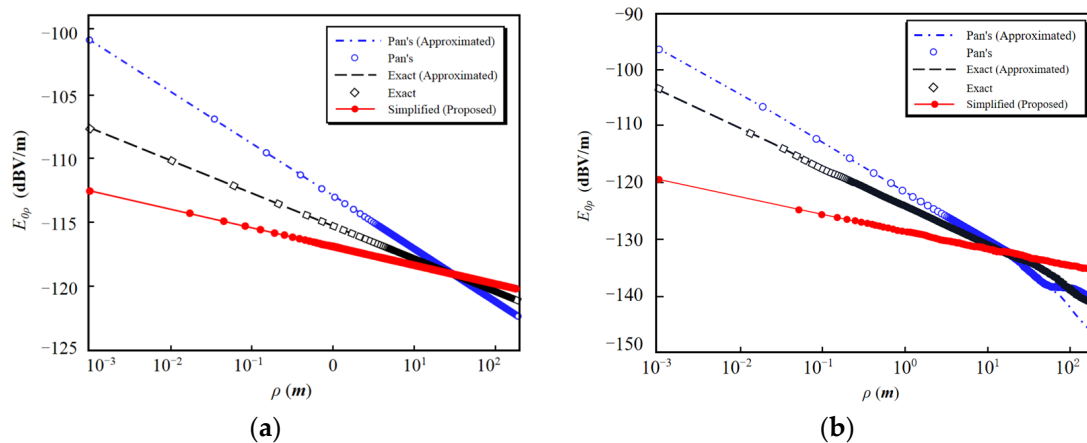


**Figure 3.** Variations in the amplitude of the near-field electric field component  $E_{0\rho}$  obtained through different methods with propagation distance ( $\varphi = 0^\circ$ ). (a)  $f = 3 \text{ Hz}$ ; (b)  $f = 30 \text{ Hz}$ .

The electric field component in the  $\rho$  direction, as calculated by different methods, gradually diminishes with increasing propagation distance. This phenomenon is linked to EMW propagation losses attributed to seawater conductivity. Notably, EMWs loosed in seawater decrease gradually with propagation distance. Additionally, at the same distance, higher frequencies lead to faster EMW decay. When the frequency remains constant, the amplitude of  $E_{0\rho}$  obtained through Pan's approximation experiences the most significant decrease with distance. In contrast, the amplitude of  $E_{0\rho}$  obtained through Margetis' exact expression falls between the results of the two approximation methods. Remarkably, the amplitude acquired through our proposed method demonstrates the gentlest decrease. Furthermore, at a frequency of 30 Hz and a propagation distance  $\rho > 50 \text{ m}$ , Pan's approximation method exhibits issues of divergence and poor stability. Conversely, both our proposed method and Margetis' exact formula maintain good stability. This clearly highlights the superiority of our proposed method over Pan's approximation. The amplitudes of  $E_{0\rho}$  derived from different methods converge in the radial direction. Figure 3 shows that electric field components in the  $\rho$  direction, calculated at 3 Hz and 30 Hz, converge at distances of 50 m and 20 m, respectively. This convergence validates the effectiveness of our proposed method within the acceptable margin of error. In summary, the analysis underscores the accuracy of our proposed method in computing near-field EMF components.

#### 4. Simulation and Analysis of Near-Region Fields

To delve deeper into the characteristics of ELF near-field distribution by an HED near the "sea-air" interface, we maintain the aforementioned relative dielectric constants for seawater and air within the cylindrical coordinate system, as shown in Figure 2. For illustration, we employ the EMF components  $E_{0\rho}$  and  $B_{0\rho}$ . Our methodology, as outlined in this paper, is used to simulate and compute the amplitude variation of these components concerning propagation distance ( $\rho$ ) across different frequencies, dipole heights, and observation point heights. The results are graphically presented in Figures 4–7.

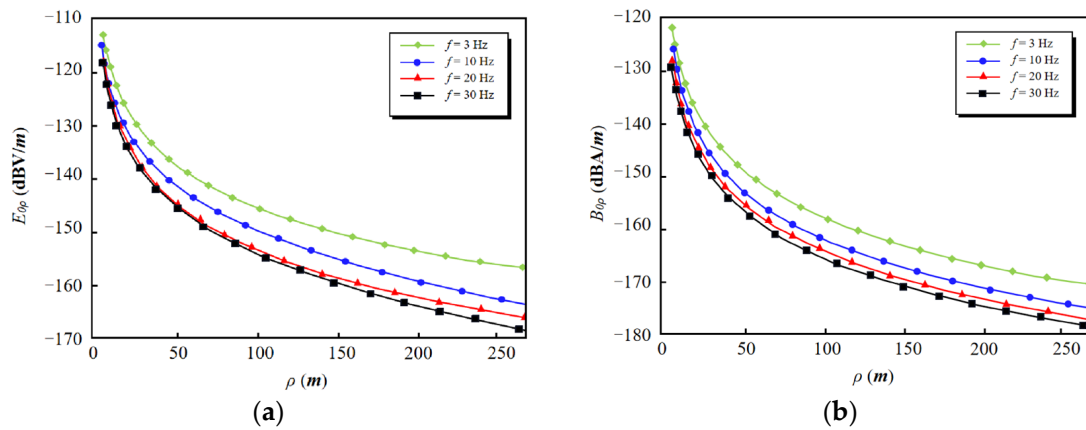


**Figure 4.** Variations in the amplitude of  $E_{0\rho}$  and  $B_{0\rho}$  components with propagation distance  $\rho$  at different operating frequencies. (a)  $E_{0\rho}$ ; (b)  $B_{0\rho}$ .

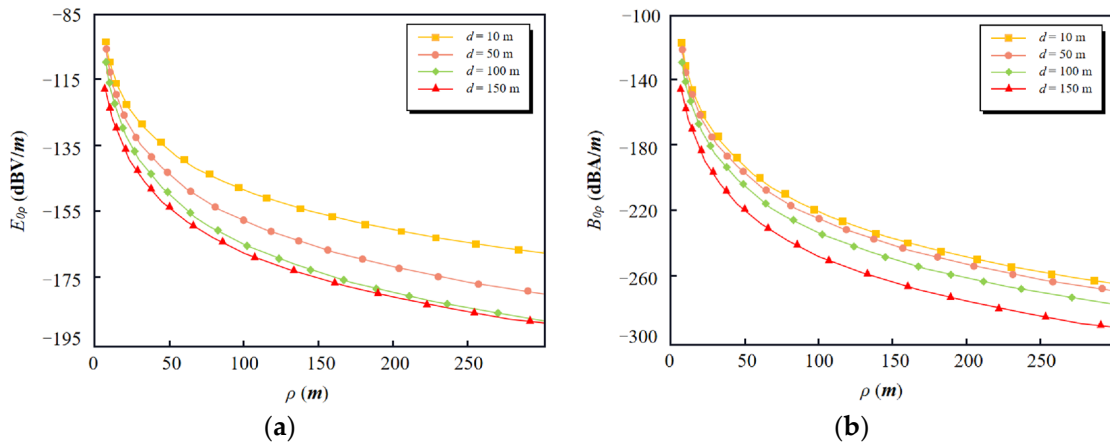


**Figure 5.** Changes of the amplitudes of  $E_{0\rho}$  and  $B_{0\rho}$  components with the propagation distance  $\rho$  at different altitudes. (a)  $E_{0\rho}$ ; (b)  $B_{0\rho}$ .

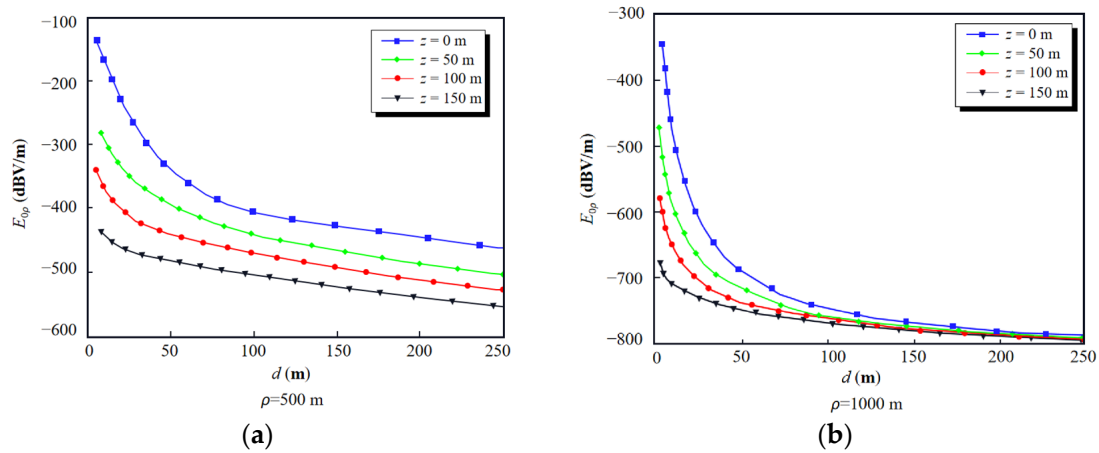


**Figure 6.** Amplitude variation of electric field component  $E_{0\rho}$  with dipole height  $d$  at different observation point heights. (a)  $\rho = 500$  m; (b)  $\rho = 1000$  m.

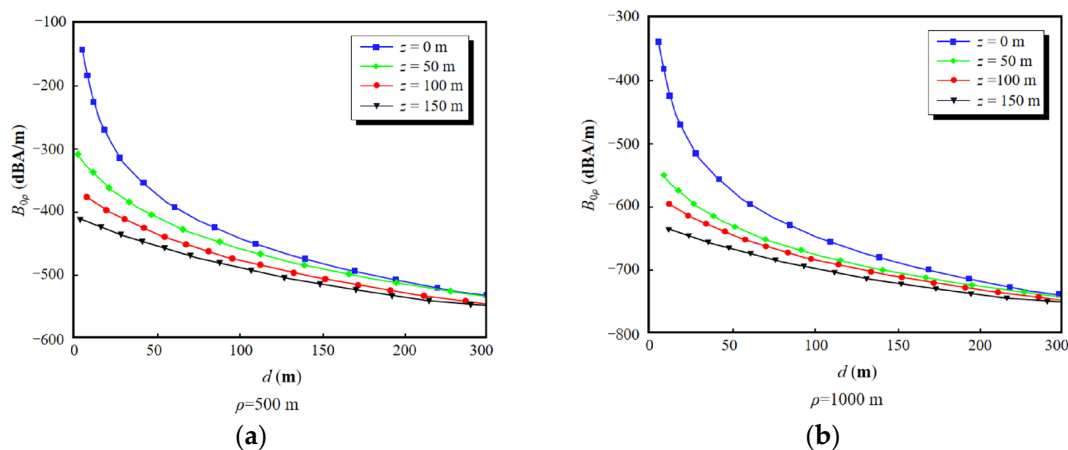


**Figure 7.** Variation of the amplitude of magnetic field component  $E_{0\rho}$  with the height  $d$  of the dipole source point at different observation points. (a)  $\rho = 500$  m; (b)  $\rho = 1000$  m.

In Figure 4a,b, the field's source and observation points are situated at distances of  $d = 10$  m and  $z = 100$  m from the sea surface, respectively. The figures illustrate the EMF components  $E_{0\rho}$  and  $B_{0\rho}$ 's trends as they relate to propagation distance ( $\rho$ ) at various operating frequencies. These graphs reveal that both the electric field component  $E_{0\rho}$  and magnetic field component  $B_{0\rho}$  decrease as horizontal distance in the  $\rho$  direction increases. When  $\rho < 50$  m, the amplitude of EMF intensity experiences the most significant changes and decays rapidly. Conversely, when  $\rho > 300$  m, the electromagnetic field intensity exhibits less substantial decay, showing a slow declining trend with an attenuation amplitude of approximately 40 dB. Additionally, it is evident that, at the same observation point, the amplitudes of EMF components  $E_{0\rho}$  and  $B_{0\rho}$  are more sensitive to changes in frequency and decrease as operating frequency increases. Notably, the reduction in amplitude is more pronounced in the high-frequency range within the ELF band, emphasizing the preference for low-frequency EMWs in seawater applications.

Figure 5a,b illustrate the variations in the electric field component  $E_{0\rho}$  and magnetic field component  $B_{0\rho}$  concerning propagation distance ( $\rho$ ) at an operating frequency of 8 Hz. The observation point's height is adjusted to align with the field source height at  $d = 10$  m, 50 m, 100 m, and 150 m, respectively. As depicted in Figure 5, the dipole's height significantly influences EMW propagation. A higher dipole source height corresponds to a more substantial attenuation in the electric field component  $E_{0\rho}$  and magnetic field component  $B_{0\rho}$ . For propagation distances ( $\rho$ ) less than 200 m, both  $E_{0\rho}$  and  $B_{0\rho}$  experience significant decreases with increasing horizontal distance. However, beyond 200 m, the field intensity amplitude stabilizes. Remarkably, near the interface, the electric field component  $E_{0\rho}$  and magnetic field component  $B_{0\rho}$  exhibit the least decline in intensity, with an attenuation amplitude of approximately 60 dB. This suggests that the attenuation rate of HED EMF components in the sea–air half-space with horizontal distance is significantly lower than in a pure seawater medium.

We further investigated the effects of varying the field source point's height on the amplitude of  $E_{0\rho}$  at observation points near the interface. Figure 6a,b depict the amplitude changes in the EMF component  $E_{0\rho}$  as the height of the field source point varies from 0 m to 300 m, with propagation distances ( $\rho$ ) set at 500 m and 1000 m and an operating frequency of 8 Hz. The source point's height significantly affects the amplitude of  $E_{0\rho}$  at observation points near the interface. Higher field source points correspond to faster attenuation rates in  $E_{0\rho}$  amplitude. However, as the source point's height increases, the attenuation rate of  $E_{0\rho}$  amplitude decreases. Notably, at a depth of  $z = 150$  m, the change in electric field component  $E_{0\rho}$  becomes less pronounced, but the attenuation value reaches its zenith. Moreover, when  $\rho = 500$  m and 1000 m, and the field source point's height is 100 m and 50 m, respectively, a distinct critical point emerges. The attenuation of  $E_{0\rho}$  remains essentially unchanged when the source height exceeds 120 m. These observations suggest

that as propagation distance ( $\rho$ ) increases, the attenuation amplitude of the electric field intensity in seawater becomes more pronounced. Specifically, when  $\rho = 500$  m, the  $E_{0\rho}$  component is effective within a dipole height of  $d = 50$  m, while for  $\rho = 1000$  m, the  $E_{0\rho}$  component is effective within a dipole height of  $d = 20$  m, offering the most favorable field intensity effects. Nonetheless, with the observation point's depth ( $z$ ) increasing, the field intensity undergoes a shift: the field intensity values gradually decrease. A critical point is reached at  $z = 150$  m, and the field strength component remains nearly constant at a dipole height of  $d = 100$  m.

As illustrated in Figure 7a,b, the magnetic field component  $B_{0\rho}$  varies with the observation point's height, exhibiting an attenuation pattern closely resembling that of the electric field intensity  $E_{0\rho}$ . The variation trend of the  $B_{0\rho}$  component at the observation point mirrors that of the  $E_{0\rho}$  component. The attenuation rate is significantly influenced by the field source point's proximity to the interface. The horizontal distance between the observation point and the field source point plays a critical role in influencing the  $B_{0\rho}$  component. Notably, when the propagation distance  $\rho = 500$  m, the  $B_{0\rho}$  component experiences its steepest decline at a dipole height of  $d = 50$  m, followed by a more gradual descent. After this initial decline, magnetic field intensity  $B_{0\rho}$  demonstrates reduced sensitivity to changes in observation point height once  $d > 200$  m. Conversely, when the propagation distance  $\rho = 1000$  m, the  $B_{0\rho}$  component exhibits pronounced changes at a dipole height of  $d = 20$  m, followed by an attenuation amplitude that remains nearly constant at a dipole height of  $d = 200$  m. These findings underscore the substantial impact of propagation distance ( $\rho$ ) on ELF antennas in seawater.

## 5. Conclusions

In this study, we established a model for the propagation of EMWs by HED at the boundary between seawater and air. By leveraging the quasi-static assumption, where  $\omega \rightarrow 0$ ,  $k_1\rho \ll 1$ , and  $k_1 \ll k_0$ , we derived integral expressions for Sommerfeld EMF in the near region induced by ELF HED in seawater. These expressions simplified the Bessel–Fourier integral terms within Sommerfeld's integral expressions, ultimately yielding the final expressions for EMF in the near region of seawater. We comprehensively analyzed the EMF propagation characteristics of an ELF HED source in seawater, taking into account different frequencies, dipole source heights, and observation point heights. Our results indicated that the electric and magnetic fields were strongest at the interface between seawater and air, with attenuation amplitudes increasing alongside higher dipole source heights, observation point heights, and propagation distances. From our simulation results, we conclude that the optimal conditions for EMF intensity occur at the seawater–air interface when the propagation distance is  $\rho = 500$  m and  $1000$  m, the dipole source height is  $d = 50$  m and  $30$  m, and the observation point depth is  $z = 150$  m and  $100$  m, respectively, within the ELF band. Beyond these conditions, the amplitude of EMF intensity becomes less responsive to changes. These findings underscore that lateral waves represent the primary propagation mode of ELF HED at the seawater–air interface. The practical applications of these conclusions hold significance in underwater communication, underwater target location, and underwater navigation. We observed consistency between our calculated results and those of Pan and Margetis, validating the accuracy of our proposed method. Notably, our method excels in predicting near-field behavior in seawater but exhibits less precision in the far-field context.

**Author Contributions:** Conceptualization, S.H. and Z.L.; methodology, H.X. and S.H.; software, H.X. and S.H.; validation, H.X. and S.H.; formal analysis, H.X. and S.H.; investigation, H.X. and S.H.; resources, S.H. and H.X.; data curation, S.H. and Z.L.; writing—original draft preparation, S.H. and Z.L.; writing—review and editing, S.H. and H.X.; visualization, S.H. and Z.L.; supervision, H.X.; project administration, H.X.; funding acquisition, H.X. All authors have read and agreed to the published version of the manuscript.

**Funding:** This research received no external funding.

**Data Availability Statement:** The data that support the findings of this study are available from the corresponding author upon reasonable request.

**Acknowledgments:** The authors thank the Naval University of Engineering Communications Engineering Laboratory for its support and assistance.

**Conflicts of Interest:** The authors declare no conflict of interest.

**Abbreviations**

- EMW Electromagnetic Wave
- EMF Electromagnetic Fields
- ELF Extremely Low Frequency
- VMD Vertical Magnetic Dipole
- HED Horizontal Electric Dipole
- HMD Horizontal Magnetic Dipole
- FFT Fast Fourier Transform

**Appendix A**

Sommerfeld numerical integral expression in seawater:

$$E_{0\rho} = -\frac{\omega\mu_0 Idl}{4\pi k_0^2} \cos \varphi \int_0^\infty \left\{ k_0^2 J_0(\lambda\rho) - \frac{\lambda^2}{2} [J_0(\lambda\rho) - J_2(\lambda\rho)] \right\} \gamma_0^{-1} e^{j\gamma_0|z-d|} \lambda d\lambda + \int_0^\infty \left\{ \frac{\gamma_0 M}{2} [J_0(\lambda\rho) - J_2(\lambda\rho)] - \frac{k_0^2 N}{2\gamma_0} [J_0(\lambda\rho) + J_2(\lambda\rho)] \right\} e^{j\gamma_0(z+d)} \lambda d\lambda \tag{A1}$$

$$E_{0\varphi} = \frac{\omega\mu_0 Idl}{4\pi k_0^2} \sin \varphi \left\{ \int_0^\infty \left\{ k_0^2 J_0(\lambda\rho) - \frac{\lambda^2}{2} [J_0(\lambda\rho) + J_2(\lambda\rho)] \right\} \gamma_0^{-1} e^{j\gamma_0|z-d|} \lambda d\lambda + \int_0^\infty \left\{ \frac{\gamma_0 M}{2} [J_0(\lambda\rho) + J_2(\lambda\rho)] - \frac{k_0^2 N}{2\gamma_0} [J_0(\lambda\rho) - J_2(\lambda\rho)] \right\} e^{j\gamma_0|z+d|} \lambda d\lambda \right\} \tag{A2}$$

$$E_{0z} = \frac{j\omega\mu_0 Idl}{4\pi k_0^2} \cos \varphi \int_0^\infty (\pm e^{j\gamma_0|z-d|} + M e^{j\gamma_0|z+d|}) J_1(\lambda\rho) \lambda^2 d\lambda \tag{A3}$$

$$B_{0\rho} = -\frac{\mu_0 Idl}{4\pi} \sin \varphi \left\{ \pm \int_0^\infty J_0(\lambda\rho) e^{j\gamma_0|z-d|} \lambda d\lambda + \int_0^\infty \left\{ \frac{M}{2} [J_0(\lambda\rho) + J_2(\lambda\rho)] - \frac{N}{2} [J_0(\lambda\rho) - J_2(\lambda\rho)] \right\} e^{j\gamma_0|z+d|} \lambda d\lambda \right\} \tag{A4}$$

$$B_{0\varphi} = -\frac{\mu_0 Idl}{4\pi} \cos \varphi \left\{ \pm \int_0^\infty J_0(\lambda\rho) e^{j\gamma_0|z-d|} \lambda d\lambda + \int_0^\infty \left\{ \frac{M}{2} [J_0(\lambda\rho) - J_2(\lambda\rho)] - \frac{N}{2} [J_0(\lambda\rho) + J_2(\lambda\rho)] \right\} e^{j\gamma_0|z+d|} \lambda d\lambda \right\} \tag{A5}$$

$$B_{0z} = \frac{j\mu_0 Idl}{4\pi} \sin \varphi \int_0^\infty [e^{j\gamma_0|z-d|} - N \cdot e^{j\gamma_0|z+d|}] \gamma_0^{-1} J_1(\lambda\rho) \lambda^2 d\lambda \tag{A6}$$

where  $r_0 = \sqrt{\rho^2 + (z - d)^2}$ ;  $r_1 = \sqrt{\rho^2 + (z + d)^2}$ . The plus and minus signs correspond to  $z > d$  and  $0 < z \leq d$ , respectively. The other variables in the above formula are consistent with those in the article.

**Appendix B**

Bessel–Fourier function integrations table:

$$\int_0^\infty J_1(\lambda\rho) e^{-\lambda z} \lambda^2 d\lambda = \frac{3\rho z}{R^5} \tag{A7}$$

$$\int_0^\infty \frac{1}{2} [J_0(\lambda\rho) + J_2(\lambda\rho)] e^{-\lambda z} \lambda^2 d\lambda = \frac{1}{\rho} \int_0^\infty J_1(\lambda\rho) e^{-\lambda z} \lambda d\lambda = \frac{1}{R^3} \tag{A8}$$

$$\int_0^\infty \frac{1}{2} [J_0(\lambda\rho) - J_2(\lambda\rho)] e^{-\lambda z} \lambda d\lambda = \begin{cases} \frac{z}{R^3} - \frac{1}{\rho^2} \left(1 - \frac{z}{R}\right) & \frac{\rho}{z} > 0.1 \\ \frac{z}{R^3} - \left(\frac{1}{2z^2} - \frac{3\rho^2}{8z^4}\right) & \frac{\rho}{z} \leq 0.1 \end{cases} \tag{A9}$$

where,  $R = \sqrt{\rho^2 + z^2}$ .

### Appendix C

The simplified Sommerfeld integral expression:

$$\begin{aligned} E'_{0\rho} &= -\frac{Idl}{4\pi\sigma_0} \cos \varphi \int_0^\infty \left\{ \frac{1}{2} [J_0(\lambda\rho) - J_2(\lambda\rho)] \right\} \cdot [e^{-\lambda|z-d|} + e^{-\lambda|z+d|}] \lambda^2 d\lambda \\ &= -\frac{Idl}{4\pi\sigma_0} \cos \varphi \left[ \frac{1}{r_1^3} \left(1 - \frac{3\rho^2}{r_1^2}\right) + \frac{1}{r_0^3} \left(1 - \frac{3\rho^2}{r_0^2}\right) \right] \end{aligned} \tag{A10}$$

$$E'_{0\varphi} = \frac{Idl}{4\pi\sigma_0} \sin \varphi \int_0^\infty \frac{1}{2} [J_0(\lambda\rho) + J_2(\lambda\rho)] (e^{-\lambda|z-d|} + e^{-\lambda|z+d|}) \lambda^2 d\lambda = \frac{Idl}{4\pi\sigma_0} \sin \varphi \left[ \frac{1}{r_1^3} + \frac{1}{r_0^3} \right] \tag{A11}$$

$$E'_{0z} = \frac{Idl}{4\pi\sigma_1} \cos \varphi \int_0^\infty (\pm e^{-\lambda|z-d|} + e^{-\lambda|z+d|}) J_1(\lambda\rho) \lambda^2 d\lambda = \frac{Idl}{4\pi\sigma_1} \cos \varphi \left[ \frac{3\rho(z-d)}{r_2^5} + \frac{3\rho(z+d)}{r_1^5} \right] \tag{A12}$$

$$\begin{aligned} B_{0\rho} &= -\frac{\mu_0 Idl}{4\pi} \sin \varphi \left\{ \pm \int_0^\infty J_0(\lambda\rho) e^{-\lambda|z-d|} \lambda d\lambda + \int_0^\infty \left\{ \frac{1}{2} [J_0(\lambda\rho) + J_2(\lambda\rho)] \right\} e^{-\lambda(z+d)} \lambda d\lambda \right\} \\ &= \begin{cases} -\frac{\mu_0 Idl}{4\pi} \sin \varphi \left[ \frac{z-d}{r_1^3} + \frac{1}{\rho^2} \left(1 - \frac{z+d}{r_0}\right) \right] & \frac{\rho}{z+d} > 0.1 \\ -\frac{\mu_0 Idl}{4\pi} \sin \varphi \left[ \frac{z-d}{r_1^3} + \frac{1}{2(z+d)^2} - \frac{3\rho^2}{8(z+d)^4} \right] & \frac{\rho}{z+d} \leq 0.1 \end{cases} \end{aligned} \tag{A13}$$

$$\begin{aligned} B'_{0\varphi} &= -\frac{\mu_0 Idl}{4\pi} \cos \varphi \left\{ \pm \int_0^\infty J_0(\lambda\rho) e^{-\lambda|z-d|} \lambda d\lambda + \int_0^\infty \left\{ \frac{1}{2} [J_0(\lambda\rho) - J_2(\lambda\rho)] \right\} e^{-\lambda(z+d)} \lambda d\lambda \right\} \\ &= \begin{cases} -\frac{\mu_0 Idl}{4\pi} \cos \varphi \left[ \frac{z-d}{r_2^3} + \frac{z+d}{r_1^3} - \frac{1}{\rho^2} \left(1 - \frac{z+d}{r_1}\right) \right] & \frac{\rho}{(z+d)} > 0.1 \\ -\frac{\mu_0 Idl}{4\pi} \cos \varphi \left[ \frac{z-d}{r_2^3} + \frac{z+d}{r_1^3} - \left( \frac{1}{2(z+d)^2} - \frac{3\rho^2}{8(z+d)^4} \right) \right] & \frac{\rho}{(z+d)} \leq 0.1 \end{cases} \end{aligned} \tag{A14}$$

$$B'_{0z} = \frac{\mu_0 Idl}{4\pi} \sin \varphi \int_0^\infty e^{-\lambda|z-d|} J_1(\lambda\rho) \lambda d\lambda = \frac{\mu_0 Idl}{4\pi} \sin \varphi \left( \frac{\rho}{r_2^3} \right) \tag{A15}$$

where  $r_0 = \sqrt{\rho^2 + (z-d)^2}$ ;  $r_1 = \sqrt{\rho^2 + (z+d)^2}$ . The plus “+” and minus “-” signs correspond to  $z > d$  and  $0 < z \leq d$ , respectively.

### References

1. Bremmer, H. The extension of Sommerfeld’s formula for the propagation of radio waves above a flat earth to different conductivities of the soil. *Physica* **1954**, *20*, 441–460. [\[CrossRef\]](#)
2. Bannister, P.R. The image theory electromagnetic fields of a horizontal electric dipole in the presence of a conducting half space. *Radio Sci.* **1982**, *17*, 1095–1102. [\[CrossRef\]](#)
3. Nazari, M.E.; Huang, W. An Analytical Solution of the Electric Field Excited by a Vertical Electric Dipole Above a Lossy Half-Space: From Radio to Microwave Frequencies. *IEEE Trans. Antennas Propag.* **2020**, *68*, 7517–7529. [\[CrossRef\]](#)
4. Akyildiz, I.F.; Pompili, D.; Melodia, T. Underwater acoustic sensor networks: Research challenges. *Ad Hoc Netw.* **2005**, *3*, 257–279. [\[CrossRef\]](#)

5. Zhu, Z.; Hu, N.; Wu, J.; Li, W.; Zhao, J.; Wang, M.; Zeng, F.; Dai, H.; Zheng, Y. A review of underwater acoustic metamaterials for underwater acoustic equipment. *Front. Phys.* **2022**, *10*, 1068833.
6. Islam, M.S.; Younis, M.F. Analyzing Visible Light Communication Through Air–Water Interface. *IEEE Access* **2019**, *7*, 123830–123845. [[CrossRef](#)]
7. Gao, X.; Liu, P.; Yin, Q.; Fu, J.W.; Hu, F.G.; Jiang, Y.; Zhu, H.B.; Wang, Y.Y. Wireless light energy harvesting and communication in a waterproof GaN optoelectronic system. *Commun. Eng.* **2022**, *1*, 16. [[CrossRef](#)]
8. Yusof, M.A.B.; Kabir, S. An overview of sonar and electromagnetic waves for underwater communication. *IETE Tech. Rev.* **2012**, *29*, 307–317. [[CrossRef](#)]
9. Singh, G.; Kumar, M. Performance analysis of electromagnetic (EM) wave in sea water medium. *Wirel. Netw.* **2020**, *26*, 2125–2135. [[CrossRef](#)]
10. Xu, H.L.; Wang, X.; Pang, M.; Ji, X.; Lin, H.; Gu, T.T. ELF Near-Field Propagation of a Vertical Electric Dipole Due to Lightning Discharges. *IEEE Trans. Antennas Propag.* **2022**, *70*, 1250–1264. [[CrossRef](#)]
11. Sommerfeld, A.N. Propagation of waves in wireless telegraphy. *Ann. Phys.* **1909**, *26*, 665–736. [[CrossRef](#)]
12. Guo, Z.; Xue, G.; Liu, J.; Wu, X. Electromagnetic methods for mineral exploration in China: A review. *Ore Geol. Rev.* **2020**, *118*, 103357. [[CrossRef](#)]
13. Füllekrug, M.; Mezentsev, A.; Watson, R.; Gaffet, S.; Astin, I.; Evans, A. Map of Low Frequency Electromagnetic Noise in the Sky: Sky Map of Electromagnetic Noise. *Geophys. Res. Lett.* **2015**, *42*, 9143–9149. [[CrossRef](#)]
14. Wang, G.; Ding, H.; Xia, H.; Wang, C. An Underwater Robot Positioning Method Based on EM-ELF Signals. In *Intelligent Robotics and Applications. ICIRA 2019. Lecture Notes in Computer Science*; Yu, H., Liu, J., Eds.; Springer: Berlin/Heidelberg, Germany, 2019; Volume 11743, pp. 643–650.
15. Moore, R.K. Radio communication in the sea. *IEEE Spectr.* **1967**, *4*, 42–51. [[CrossRef](#)]
16. Birsan, M. Measurement of the extremely low frequency (ELF) magnetic field emission from a ship. *Meas. Sci. Technol.* **2011**, *22*, 085709. [[CrossRef](#)]
17. Margetis, D.; Wu, T.T. Exactly calculable field components of electric dipoles in planar boundary. *J. Math. Phys.* **2001**, *42*, 713–745. [[CrossRef](#)]
18. Banos, A. *Dipole Radiation in the Presence of a Conducting Half-Space*; Pergamon Press: Oxford, MA, USA, 1966.
19. Wait, J.R. *Electromagnetic Waves in Stratified Media*; IEEE Press: Piscataway, NJ, USA, 1966.
20. Kraichman, M.B. *Handbook of Electromagnetic Propagation in Conducting Media*; US Government Printing Office: Washington, DC, USA, 1976.
21. King, R.W.P. *Lateral Electromagnetic Waves*; Springer: New York, NY, USA, 1992.
22. Pan, W.Y. *LF VLF ELF Wave Propagation*; The University of Electronic Science and Technology Press: Chengdu, China, 2014.
23. Bush, B.; Tripp, V.; Naishadham, K. Practical modeling of radio wave propagation in shallow seawater. In Proceedings of the IEEE Antennas and Propagation Society International Symposium (APSURSI), Chicago, IL, USA, 8–14 July 2012.
24. Bishay, S.T.; Abo-Seida, O.M.; Shoeib, H.S. Wave propagation in air from a vertical magnetic Ndipole located in three rough-layered structures. *J. Electromagn. Waves Appl.* **2013**, *27*, 911–929. [[CrossRef](#)]
25. Wang, J.; Chen, J. The application of complex image theory in rapid simulations of electromagnetic logging while drilling in unparallel layered formation. In Proceedings of the 2016 IEEE International Symposium on Antennas and Propagation (APSURSI), Fajardo, PR, USA, 26 June–1 July 2016.
26. Yang, Y.L.; Li, X.; Ding, S.H.; Wang, W.S. A numerical algorithm for arbitrary real-order Hankel transform. *Wuhan Univ. J. Nat. Sci.* **2022**, *27*, 26–34. [[CrossRef](#)]
27. Wang, H.L.; Yang, K.D.; Zheng, K. Electromagnetic field radiated in air from a horizontal/vertical magnetic dipole in sea. *J. Electromagn. Waves Appl.* **2015**, *29*, 858–873. [[CrossRef](#)]
28. Wang, J.H.; Li, B. Electromagnetic fields generated above a shallow sea by a submerged horizontal electric dipole. *IEEE Trans. Antennas Propag.* **2017**, *65*, 2707–2712. [[CrossRef](#)]
29. Xu, H.L.; Gu, T.T.; Li, K. Approximated solutions for ELF near-field propagation due to a horizontal electric dipole excitation near the sea-rock boundary. *IEEE Trans. Antennas Propag.* **2018**, *66*, 2471–2481. [[CrossRef](#)]
30. Peng, H.Y.; Chen, Y.; Wang, Y.X.; Zhang, S.T.; Mao, Y.Z. Low frequency fields excited by a horizontal magnetic dipole near boundary of lossy half-space. In Proceedings of the 2018 12th International Symposium on Antennas, Propagation and EM Theory (ISAPE), Hangzhou, China, 3–6 December 2018.
31. Shoaib, H.S. Electromagnetic field analysis of a vertical magnetic dipole antenna in planar multi-layered media. *IETE Tech. Rev.* **2020**, *38*, 357–364. [[CrossRef](#)]
32. Zeng, H.R.; He, T.; Li, K. Mode theory and propagation of ELF radio wave in a multilayered oceanic lithosphere waveguide. *IEEE Trans. Antennas Propag.* **2021**, *69*, 5870–5880.
33. Xu, H.; Gu, T.; Zhu, Y.; Wei, X.; Li, L.; Yin, H. Communication with a magnetic dipole: Near-field propagation from air to undersea. *IEEE Trans. Antennas Propag.* **2021**, *69*, 1052–1064. [[CrossRef](#)]
34. Hu, S.M.; Xie, H.; Ding, T. Electromagnetic field variation of ELF near-region excited by HED in a homogeneous half-space model. *Appl. Sci.* **2023**, *13*, 7499. [[CrossRef](#)]
35. Tasic, M.S.; Kolundzija, B.M. Method of Moment weighted domain decomposition method for scattering from large platforms. *IEEE Trans. Antennas Propag.* **2018**, *66*, 3577–3589. [[CrossRef](#)]

36. Tran, T.H.; Baba, Y.; Somu, V.; Rakov, V.A. FDTD Modeling of LEMP Propagation in the Earth-Ionosphere Waveguide with Emphasis on Realistic Representation of Lightning Source. *J. Geophys. Res. Atmos.* **2017**, *122*, 12918–12937. [[CrossRef](#)]
37. Gradshteyn, I.S.; Ryzhik, I.M. Definite Integrals of Special Functions. In *Table of Integrals, Series, and Products*, 8th ed.; Zwillinger, D., Moll, V., Eds.; Academic Press: Pittsburgh, PA, USA, 2014; pp. 637–775.

**Disclaimer/Publisher’s Note:** The statements, opinions and data contained in all publications are solely those of the individual author(s) and contributor(s) and not of MDPI and/or the editor(s). MDPI and/or the editor(s) disclaim responsibility for any injury to people or property resulting from any ideas, methods, instructions or products referred to in the content.